Evolutionary Approach for Detection of Buried Remains Using Hyperspectral Images

León Dozal, José L. Silván-Cárdenas, Daniela Moctezuma, Oscar S. Siordia, and Enrique Naredo

Abstract

Hyperspectral imaging has been successfully utilized to locate clandestine graves. This study applied a Genetic Programming technique called Brain Programming (BP) for automating the design of Hyperspectral Visual Attention Models (H-VAM.), which is proposed as a new method for the detection of buried remains. Four graves were simulated and monitored during six months by taking in situ spectral measurements of the ground. Two experiments were implemented using Kappa and weighted Kappa coefficients as classification accuracy measures for guiding the BP search of the best H-VAM. Experimental results demonstrate that the proposed BP method improves classification accuracy compared to a previous approach. A better detection performance was observed for the image acquired after three months from burial. Moreover, results suggest that the use of spectral bands that respond to vegetation and water content of the plants and provide evidence that the number of buried bodies plays a crucial role on a successful detection.

Introduction

Locating unmarked graves represents a complicated and time-consuming forensic problem because their locations are often remote and the burial time is generally unknown (Siegel and Saukko, 2013). The research on the detection of clandestine graves through multi and hyperspectral images is incipient, yet has proven to be one of the most challenging forensic problems. This is an important area of work, since airborne hyperspectral data enable searching over a large area that is otherwise inaccessible by foot; especially because, in principle, any area of the Earth can be mapped by hyperspectral imaging, be it with aircraft or satellites (Ross *et al.*, 2005).

Several studies have tested the potential of multispectral and hyperspectral images with varying results. Kalacska and Bell (2006) were among the first that demonstrated the potential of remote sensing as a tool for locating heretofore unknown mass graves. Afterwards, Kalacska *et al.* (2009) analyzed the *in situ* and airborne spectral reflectance of a set of animal mass graves and identically constructed false graves. Their results indicated that the reflectance spectra of grave are readily distinguishable from false grave at both scales. In addition, they observed that vegetation regeneration was severely inhibited by cattle carcasses for up to a period of 16 months. Caccianiga *et al.* (2012) studied the effects of decomposition of buried swine carcasses on soil and vegetation structure and composition as a tool for detecting clandestine graves. They found that soil disturbance was the main factor affecting plant cover, while the role of decomposition seemed to be much less critical. Leblanc *et al.* (2014) performed a blind-test of the potential for airborne hyperspectral imaging technology to locate buried remains of pig carcasses. They were able to predict two single graves, within GPS error (10 m), whose location they did not know. Recently, Silván-Cárdenas *et al.* (2017) studied some methods for detecting clandestine graves using hyperspectral data collected on ground. Through a controlled experiment using buried carcasses of pigs, demonstrated that hyperspectral data have potential for detecting buried remains only after three months from burial. Furthermore, that the critical spectral regions for graves detection are the NIR and SWIR1[1] spectral regions, some of which were so narrow (10 nm) that stressed the need for hyperspectral sensing.

The method of acquisition of hyperspectral images is equally important than the process of pattern recognition for detection of graves based on such information. In this sense, some techniques of evolutionary computation have been successfully applied for selection and combination of spectral bands aiming at different applications such as classification of vegetation species, soil mineral identification, synthesizing spectral indices, estimate pasture mass and quality, and precision farming, to mention just a few (Ross *et al.*, 2005; Chion *et al.*, 2008; Albarracín *et al.*, 2016; Zhuo *et al.*, 2008; Li *et al.*, 2011, Kawamura *et al.*, 2010, Puente *et al.*, 2011, Ullah *et al.*, 2012, Davis *et al.*, 2006, Landry *et al.*, 2006; Kawamura *et al.*, 2010; Awuley and Ross, 2016). On the other hand, currently, visual attention models have been designed for the spatial and spectral analysis of hyperspectral images with applications such as detection of prominence, visualization and interpretation, and detection of objects (Le Moan *et al.*, 2011and 2013; Wang, 2013; Liang *et al.*, 2013; Cao *et al.*, 2015; Zhang *et al.*, 2017).

In this study an evolutionary technique is proposed based on genetic programming, known as Brain Programming (BP), for optimizing a so-called Hyperspectral Visual Attention Models (H-VAM) for graves detection.

Problem Statement

The present work addresses the problem of detection of clandestine graves as a problem of classification of hyperspectral images. The image classification problem can be stated in formal terms as follows. Suppose we want to classify each pixel in an image into one of N classes, let say C_1, C_2, …, C_N. Then, decision rules must be established to enable assignment of any given pixel to these classes (Varshney and Arora, 2004).

When working with hyperspectral images, some issues arise due to the high dimensionality of this type of images, e.g., Hughes phenomenon, high information redundancy in spectral and spatial domains, need for finding features that increase discrimination between classes and high computational resources required in the classification process.

For this reason, a compelling need to reduce the dimension of data exists. The methods for reduction of dimensionality can be roughly divided into two categories: feature extraction

Centro de Investigación en Geografía y Geomática "Ing. Jorge L Tamayo" A.C., Circuito Tecnopolo Norte No. 117, Fracc. Tecnopolo II, Pocitos, Aguascalientes, CP 20313, Mexico (leon.dozal@gmail.com).

Photogrammetric Engineering & Remote Sensing
Vol. 84, No.7, July 2018, pp. 19–xxx.
0099-1112/18/19–xxx

doi: 10.14358/PERS.84.7.xxx

1. The abbreviations used in this paper are summarized in Table 1.

and feature selection (Li *et al.*, 2014). The former refers to a process to transform the high-dimensional feature space to a low-dimensional space through linear or no linear combinations of original bands. Whereas, the latter refers to a selection of an optimal subset of features, through a combinatorial optimization (Yoon and Park, 2015). At this point, it should be noted that classification accuracy is highly impacted by feature selection or extraction methods.

In this study, we tested the BP algorithm as a feature selection method. Much research has been done about feature selection from an evolutionary computation approach (see the Brain Programming Implementation Section), but little work has been done around feature extraction methods incorporating both spatial and spectral information through such approach. In order to integrate spectral and spatial information in our solution to the grave detection problem, we use an H-VAM optimized with a BP algorithm. The H-VAM allows building a saliency map that corresponds to a classified image.

Visual Attention from a Computational Standpoint

The concept of visual attention or visual saliency comes from the study of the human visual system and this consists in the ability to efficiently find objects or regions that stand out relative to their neighboring parts in a scene (Borji and Itti, 2013). Therefore, visual attention is an inherently active and selective process by which people attend to a subset of the available information for further processing along the visual pathway (Zhang *et al.*, 2008). For this reason, when it comes to computer science, the notion of saliency is closely related to visual attention in color or gray scale images (Le Moan *et al.*, 2013). In a broad sense, the concept of saliency is not exclusive of the vision process. Recently, Le Moan *et al.* (2013) coined the term "spectral saliency" to name the extent to which a certain group of pixels stands out in an image, in terms of reflectance rather than in terms of colorimetric attributes. In principle, any kind of data can be considered, although, until now, only a few studies have used other than visible spectrum images.

In 1998, the first computer models of visual attention appeared. The most influential model has been that of Itti *et al.* (1998); they introduced the concept of "saliency map" that is an image in gray scales where the larger the value of a pixel, the more prominent it is. Since then, the saliency map has been utilized in various applications, such as object recognition, object detection, segmentation, and tracking. The reader is referred to (Borji and Itti, 2013) for a comprehensive review of the state of the art in visual attention modeling. There is a growing interest in using saliency attention models for multi and hyperspectral images. Considering the high dimensionality of hyperspectral images, traditional Visual Attention Model (VAM), such as that of Itti *et al.* (1998), cannot be directly applied to hyperspectral imagery (Cao *et al.*, 2015). Nowadays, there are few VAMs dealing with the spectral saliency (Le Moan *et al.*, 2011and 2013; Wang, 2013; Liang *et al.*, 2013; Cao *et al.*, 2015; Zhang *et al.*, 2017).

Most of the methods adopted saliency detection based on spectral signatures. In this way, feature extraction is only operated in the spectral domain, but the spatial distribution of targets has not been fully explored. However, the spatial distribution has proved to be very valuable for image analysis in remote sensing and computer vision communities (Cao *et al.*, 2015).

Introduction to Brain Programming

Brain Programming (BP) is an evolutionary computing technique based on Genetic Programming (GP), which is a technique to solve optimization problems based on Darwin's theory of evolution; and the well-known principle of natural selection, proposed by Koza (1992).

Table 1. Abbreviations used in this paper.

BP	Brain Programming
BSM	Binary Saliency Map
CM	Conspicuity Map
EFI	Evolved Feature Integration
EVO	Evolved Visual Operator
FI	Feature Integration
GP	Genetic Programming
H-VAM	Hyperspectral Visual Attention Model
MIR	Middle-InfraRed (1300-2500 nm)
MM	Mathematical Morphology
NDSI	Normalized Difference Spectral Index
NIR	Near-InfraRed (701-1000 nm)
OA	Overall Accuracy
PLS	Partial Least Squares
SE	Structuring Element
SI	Spectral Index
SM	Saliency Map
SWIR1	Short-Wave InfraRed (1001-1800 nm)
SWIR2	Short-Wave InfraRed (1801-2500 nm)
VAM	Visual Attention Model
VIP	Variable Importance of Projection
VM	Visual Map
VNIR	Visible and Near-InfraRed (350-1000nm)
VO	Visual Operator

BP evolves parts of computer programs, in this case, parts of the H-VAM. The evolvable parts of the H-VAM are represented as syntax tree structures that can solve a particular sub-problem, these structures are known as individuals. BP starts with an initial population of individuals that are randomly generated. Each tree that is part of the individual is produced from a set of functions, $F = \{f_1, f_2, \ldots, f_n\}$ and a set of terminals $T = \{t_1, t_2, \ldots, t_n\}$. It is important to note that each tree can have different sets F and T, unlike GP; this allows the function specialization of each tree. Functions correspond to nodes with children in the tree whereas terminals correspond to leaves in the tree. The randomly generated initial population is evolved to find new individuals that can give a better solution to a particular problem. First, individuals are evaluated using a fitness function. Besides, the fitness function is defined as a criterion for reproduction probability, each individual is given a probability for reproduction directly proportional to its fitness. Next, individuals are selectively recombined according to their probability of reproduction to produce a new population of potentially better individuals. These new individuals are created by means of operations called genetic operators, which are applied with an a priori probability. The principal genetic operators in BP are chromosomal crossover (two individuals exchange complete trees), gene crossover (two individuals exchange a sub-tree of each of their trees), chromosomal mutation (one individual arbitrarily changes each one of its trees by a new one randomly generated) and gene mutation (one individual arbitrarily changes one sub-tree of each one of its trees by a new one randomly generated). For a more detailed explanation of genetics operations of BP see (Dozal *et al.*, 2014). During evolution, each new iteration, known as generation, will contain improved solutions and the

process is repeated until some stop criterion is met. This may be a pre-specified level of fitness, convergence, or a maximum number of generations (Davis *et al.*, 2006).

The primary objective of BP is to be able to simply define a task and have the machine independently learn to perform it. BP provides the framework for the machine to evolve its own algorithms, delivering a solution as a computer program or as data representing a computer program (Banzhaf *et al.*, 1998).

In this way, GP has been very successful at evolving novel and unexpected ways of solving problems, generally producing a number of instances that are competitive with human-produced results (Koza, 2010). The GP paradigm is worth exploring because it lends itself well to feature extraction in combination with feature selection (Iglesia, 2013). The executable nature of the evolved individuals makes GP ideally suited for implementing multispectral analysis and other remote sensing applications, such as classifiers and mathematical indices that enhance the signal of several features over the Earth's surface by means of supervised learning approaches (Agnelli *et al.*, 2002). For a more detailed description of the BP approach see (Dozal *et al.*, 2014).

Materials and Methods

Field Data Collection

Four graves were simulated in a terrain near to Yautepec, Morelos, México. The terrain was divided into a grid of 19-by-19 squares. Ten carcasses of pigs (pietrain breed) were distributed into four graves. The spatial distribution of these graves is shown in Figure 1 with labels F2, F4, F6, and F7. Each grave size is 2 m-by-2 m wide by 1.1to 1.5 m depth. Carcasses were distributed as shown in Table 2. In addition to these four graves, three empty pits were created with the same dimensions, in order to simulate soil disturbances caused by other non-burial process such as plow or constructions. The graves were kept undisturbed during the whole six months measurement period.

After burial, from 12 February to 29 July 29, the soil reflectance was measured every fourteen days approximately, by using a full-range field spectroradiometer (Field Spec 4 Std Res by ASD Inc. @ 350-2500nm) in each one of the 19-by-19 squares. Measurements were taken using the natural illumination, the time of data acquisition was approximately within 11:00 and 13:00 hours local time so that the sun position did not vary a lot, and whenever the sky conditions was clear or mostly clear, the winds blew slowly (0 to 5 kmh), and there was no rainfall. As a result, twelve hyperspectral images (H_I) were formed with the ground sampling distance of 1 m. By July, the vegetation had already over passed the mesh height so that some measurements were carried out under the canopy of vegetation. This was actually the main reason to stop monitoring, as measurements under the canopy are not compatible with airborne or satellite measurements (Silván-Cárdenas *et al.*, 2017).

After the acquisition of the ground measurements, the data were preprocessed prior to classification; this process is explained in the next Section.

Hyperspectral Image Preprocessing

Before analyzing the data for classification and graves detection, it is necessary to apply a preprocessing due to technical conditions we describe next. A spectral misalignments occurs because the spectroradiometer combines three sensors for the measurement of the spectral signature, that are, VNIR: 350-1000 nm, SWIR1: 1001-1800 nm and SWIR2: 1801-2500 nm, this is 2,151 bands. If the spectroradiometer is not warmed up sufficiently, the measurements around the edge of the spectral regions of the three sensors do not match. This was observed only in a couple of images and the problem was corrected by fixing

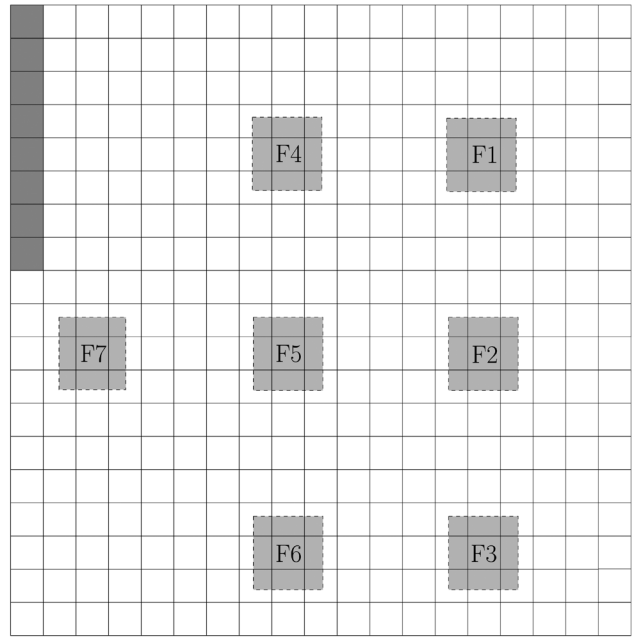

Figure 1. Spatial distribution of graves.

Table 2. Distribution of carcasses in the graves.

Grave ID	Depth [m]	No. Carcasses	Weight [Kg]
F1	1.2	0	0
F2	1.2	3	255
F3	1.5	0	0
F4	1.0	2	170
F5	1.1	0	0
F6	1.2	1	85
F7	1.1	4	340

the spectral region of VNIR sensor and applying an offset to the reflectance captured by the SWIR1 and SWIR2 sensors. Another problem derived from bad calibration and changing light conditions is banding; some images presented this issue in which the pixels of an entire line appear lighter or darker than those of neighbor lines. This was corrected by multiplying the reflectance values of banding line by a coefficient that was estimated using the average reflectance of neighbor lines. It is a common practice to eliminate spectral bands of low atmospheric transmissivity in which reflectance values fluctuate erratically. Such bands are: 1350-1480 nm, 1780-2032 nm and 2450-2500 nm, the incident radiation on the soil, in these wavelengths, is almost null because water vapor absorbs almost completely the electromagnetic radiation. Finally, due to the changing illumination conditions among the measurements it becomes necessary to normalize them. We identified a location in the grid that fells on a piece of concrete, such location was considered as reflectance invariant through the time. Normalization consisted on adjusting the spectral range from 400 to 500 nm (blue band) of all images at that location. Taking as reference the first image acquired on 12 February, images were re-calibrated through the empirical line method, so that following calibration all images presented similar reflectance in the blue band for the spectrally-invariant point (Silván-Cárdenas *et al.*, 2017). Images are hereafter identified by acquisition date in the format MMDDYY.

The H-VAM Algorithm

This study proposed a modified VAM (H-VAM) based on the Itti *et al.* (1998) model. We adapted the model to the intrinsic characteristics of H_Is. Therefore, the H-VAM algorithm is an abstraction of the natural process of visual attention, which

can be applied to find the location of buried remains in a hyperspectral image.

The H-VAM algorithm takes advantage of the knowledge about the task to be performed and the intrinsic properties of the objects in the scene, such as spectral reflectance. The H-VAM program is based on specialized functions, known as visual operators, which are in charge of extracting characteristics of the observed scene and also of its subsequent combination. All this, for highlighting the necessary information for the task at hand, in this case the detection of buried remains. Figure 2 shows the diagram of the H-VAM algorithm, which is explained in detail in the following subsections.

Feature Extraction and Visual Maps

As stated in Figure 2 the scene recorded through a full-range spectroradiometer corresponds to a H_I with 1,719 wavelengths, which is input to the H-VAM algorithm. The H_I is used to extract different kinds of characteristics by using specialized operators according to the type of information to be extracted.

The matter of how spectral variations are represented mathematically and conceptually is an important first step in defining how the extraction of the desired information should proceed (Landgrebe, 1999). In this trace, the present study tackles feature extraction from both the spectral and spatial domains. The feature extraction of H-VAM algorithm is implemented through functions called Visual Operators (VO). These are mathematical functions, which are in charge to process the H_I with the aim of extract specific characteristics in the form of spectral or spatial features. Each VO is defined as a transformation VO_d: $H_I \rightarrow VM_d$ where H_I represents the input and VM_d is the resulting image, known as visual map, along a spectral or spatial domain d.

In this study, H_Is are defined as: $H_I = \{\rho_\lambda \mid \lambda \in W\}$ where ρ_λ is the reflectance value for a wavelength λ and W is the wavelength region ranging from 350 nm to 2,500 nm with a resolution of 1 nm; thus H_I is conformed by a grid of 19-by-19 pixels and 1,719 spectral bands. In the first place, the input image H_I is transformed by a VO resulting in a Visual Map (VM). It is important to realize that the transformed images VM_d may not retain the physical interpretation as the input reflectance image (Li *et al.*, 2014). The structure of $VO_{spectral}$ and $VO_{spatial}$ is described in the followings sections.

Spectral Features Extraction

The spectral feature extraction is in charge to obtain information from the relationships among spectral bands. It is possible to obtain a lot of information by combining spectral bands; the wavelength relationship between bands can be as important as the reflectance value of the bands (Khanna *et al.*, 2007). The relations among spectral responses to different wavelengths are defined by mathematical transformations. The spectral indices are a good example; they are based on combinations of two or more bands that enhance specific spectral properties. Remote sensing experts analyze the reflectance properties of Earth's surface and the relationships between bands instead of the absolute value of reflectance at any one of those bands, then they design indices to extract information to characterize it (Khanna *et al.*, 2007). From a computational standpoint, the operator $VO_{spectral}$ states a transformation from the H_I to a visual map $VM_{spectral}$, and it is defined as follows:

$$VO_{spectral} : H_I \rightarrow VM_{spectral} \; . \tag{1}$$

The pixel values of the resulting $VM_{spectral}$ represent the prominence of the extracted spectral features.

Spatial Features Extraction

In this study, the spatial feature extraction refers to the process specialized on obtaining morphological intrinsic features from the objects in the image, in other words, the structural information. Spatial information comprises: edge detection, suppression of selected image structures based on shape, orientation, and size criteria, among others. Accordingly, this method searches for objects with a specific spatial arrangement of pixels rather than single pixels with a specific spectral signature (Soille and Pesaresi, 2002). Mathematical morphological operators can tackle the analysis of spatial data in an image. According to Soille (2003), Mathematical Morphology (MM) can be defined as a theory for the analysis of spatial structures. In this sense, the extensive use of MM in geosciences and remote sensing research areas has proved as a powerful tool for the spatial analysis of H_I s and for a wide range of applications such as segmentation of high resolution satellite imagery (Pesaresi and Benediktsson, 2001); extraction of information about size, shape and the orientation of image structures in single-band remote sensing of urban areas (Benediktsson *et al.*, 2003); segmentation and classification of hyperspectral images (Tarabalka *et al.*, 2010; Noyel *et al.*, 2007; Plaza *et al.*, 2009); to mention a few examples. For a comprehensive survey of literature regarding the use of MM in the field of geoscience and remote sensing, see Soille and Pesaresi (2002).

Former methods to analyze hyperspectral data were focused on a per-pixel processing, by merely utilizing the spectral information from thousands of spectral channels. A major weakness of such methods is the lack of information about the spatial organization of the pixels as hyperspectral data are not treated as images (Plaza *et al.*, 2009). Later, with the aim to improve the results obtained by processing techniques of hyperspectral data, many studies remarked on the importance of integrating the spatial information (Plaza *et al.*, 2009; Tarabalka *et al.*, 2010).

In this work, the $VO_{spatial}$ is defined as follows:

$$VO_{spatial} : H_I \rightarrow VM_{spatial} \; . \tag{2}$$

The pixel values of the resulting $VM_{spatial}$ represent the prominence of the extracted spatial features.

Once the VMs are obtained, the H-VAM must compute an additional map, known as Conspicuity Map (CM), for each feature domain. The computation of CMs is as in Walther and Koch (2006) model and they are obtained by means of a center-surround function. Its main task is to measure the differences between firing rates at the center (c) and surroundings (s) of the VMs with the aim of making the feature extraction scale-invariant and normalizing CMs. The H-VAM utilizes

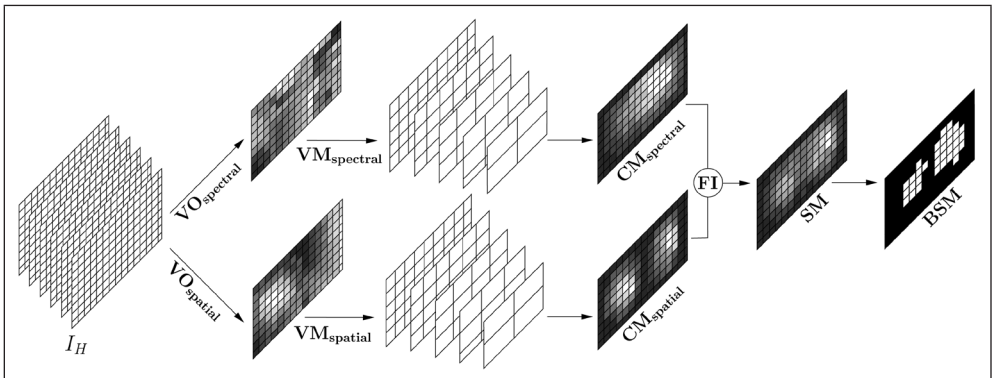

Figure 2. Diagram of the H-VAM algorithm.

values of c = {1, 2, 3} and s = {c + 1, c + 2}. At this point, we have $CM_{spectral}$ and $CM_{spatial}$ normalized. After that, the H-VAM model combines the CMs to obtain a single saliency map as explained next.

Feature Integration and Saliency Map

The final stage of the H-VAM process is the fusion of features into one single Saliency Map (SM). The combination of CMs is a hard problem because CMs belong to different and unrelated features. We consider that the problem must be addressed regarding the purpose of the task at hand. Indeed, in this work we adopted a goal-driven paradigm to guide the search of a suitable combination of features, where the main criterion to guide the suitable combination of characteristics is the classification accuracy. The integration of CMs is accomplished by means of a Feature Integration operator, FI, as follows:

$$\text{FI} : \text{CM}_{spatial} \times \text{CM}_{spectral} \rightarrow \text{SM} . \quad (3)$$

As a result, SM represents the prominence of the combined features, understood as a function of the extracted features. Finally, SM is binarized (BSM) using a prominence threshold equal to zero, $th = 0$. All values of pixels that are less or equal to zero are assigned the value of 0, while those greater than zero are assigned the value of 1. This binarization allows to compare, in a direct way, the BSM with the binary image of ground truth.

Brain Programming Implementation

This section describes the details of the implementation of BP for this particular problem. There are some works related with classification of multi- and hyperspectral images, which utilize evolutionary computation techniques as genetic algorithms (Zhuo *et al.*, 2008; Li *et al.*, 2011; Kawamura *et al.*, 2010; Ullah *et al.*, 2012) and genetic programming (Davis *et al.*, 2006; Landry *et al.*, 2006; Awuley and Ross, 2016).

Genetic Representation of the H-VAM

In this paper, the genotype, namely computational representation of an H-VAM, is represented with a triplet of trees (Figure 3). In this way, all possible combinations of terminals and functions represent the search space of the problem. As we mentioned before, BP algorithm is designed to deal with arrays of specialized trees, unlike GP. The term "specialized" refers to the fact that each tree in the genotype has its own sets of functions and terminals that were carefully chosen according to the desired kind of features we attempt to extract. This allows each tree to concentrate in the extraction of specific characteristics, such as spectral or spatial features, or in the fusion of both. The main idea is to evolve $VO_{spectral}$, $VO_{spatial}$, and FI operators, thereby, each one of the trees encodes one operator. In the rest of the paper we will refer to such encoded operations as Evolved Visual Operators (EVO) and Evolved Feature Integration (EFI). Below, we detail the genotype structure, including both EVOs and EFI, according to the features they extract.

Extraction of H-VAM Spectral Features

The operator $EVO_{spectral}$ is in charge of extracting information derived from the spectral signature. For this reason we included to the set of terminals, which is expressed by $T_{spectral}$, the spectral responses in the wavelength range from 350 nm to 2500 nm with a resolution of 1 nm, that is to say, 1,719 spectral images, represented by H_I, after removing the bands of low transmissivity. These terminals could be sufficient but, with the purpose of exploit *a priori* knowledge about wavelengths relations, we decided to add some Spectral Indexes (SI) to the list of terminals. Table 3 lists the SIs that serve as terminals for $EVO_{spectral}$, their formula and a brief description of what they were made for.

Spectral indices can be formally defined as follows:

$$\text{SI} = \text{H}_\text{I}(x, y, \lambda) \rightarrow \Re \quad (4)$$

where $H_I(x, y, \lambda)$ is the spectral value of a pixel located at x, y coordinates in the spectral image corresponding to λ wavelength. Hence, SIs can be seen as pixel-wise functions that associate spectral bands with a scalar from which the pixel class is determined (Albarracín *et al.*, 2016). In general, any linear or nonlinear combination of spectral responses at relevant wavelengths can be considered as a spectral index.

In addition, it is necessary to fix the set of functions that determine the relationship among terminals. The function set of $EVO_{spectral}$, $F_{spectral}$, is shown in Table 4, most of them appear in the formulas of the spectral indices in Table 3. The functions: $+k$, $-k$, $\times k$, $\div k$, $\sqrt[k]{}$, $()^k$, represent the signalized arithmetic operations where one of the terms is a constant k with random values ranging from 0 to 100. Finally, we added the Normalized Difference Spectral Index (NDSI) defined as $NDSI = (\rho_1 - \rho_2)/(\rho_1 + \rho_2)$ where ρ_1 and ρ_2 are spectral responses at different wavelengths. This normalization is practical for reducing atmospheric disturbance or other error sources as well as for enhancing and standardizing the spectral response to observed targets. In principle, NDSIs with consecutive wavelengths is similar to the first derivative up to a normalization factor (Ionue *et al.*, 2008).

Similarly to SIs, all EVOs are operations defined at pixel level, this means, we apply the function to the corresponding pixels of two spectral images. Thus, all these functions are defined pixel to pixel. Most of the time SIs are designed by specialists, with BP approach the SI creation is automated. As we mention in the first Section, similar approaches have been made in the past (Smith and Bull, 2005; Chion *et al.*, 2008; Albarracín *et al.*, 2016).

Next, we explain the extraction of spatial features and its relationship with mathematical morphology.

Extraction of H-VAM Spatial Features

Contrary to $EVO_{spectral}$, $EVO_{spatial}$ are neighborhood-based operators and they are designed to extract spatial information from H_Is. Unsurprisingly, the set of terminals of $EVO_{spatial}$ operators, known as $T_{spatial}$, is compounded by H_I wavelengths. On the other hand, the set of functions, $F_{spatial}$, is conformed by the morphological operations showed in Table 5, as we

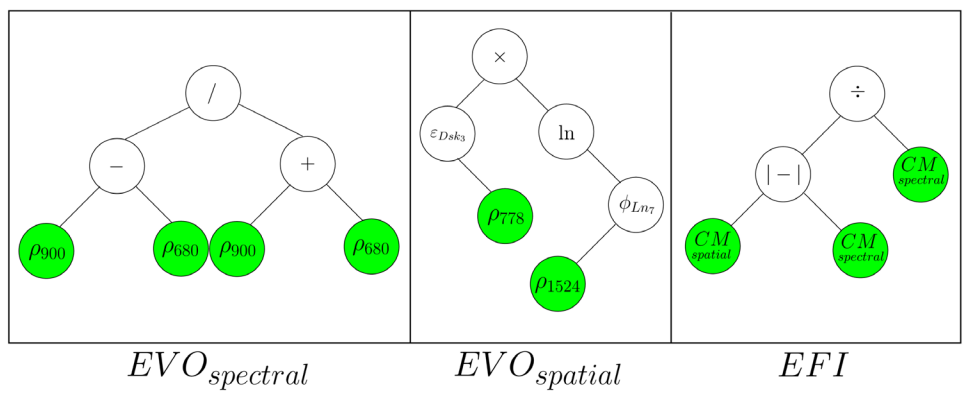

Figure 3. Example of a H-VAM's genotype.

Table 3. Spectral indices that are part of terminals set, T_{spectral}, of $\text{EVO}_{\text{spectral}}$.

Spectral Indices	Formulation	Estimation
Atmospherically Resistant Vegetation Index	$ARVI = -0.18 + 1.17 * NDVI(\rho_{830}, \rho_{660})$	Vegetation. It has self-correction properties for the atmospheric effects (Kaufman and Tanré, 1992).
Enhanced Vegetation Index	$EVI = 2.5\frac{(\rho_{859}, \rho_{645})}{(\rho_{859} + 6 * \rho_{645} - 7.5 * \rho_{469} + 1)}$	Vegetation. It is sensible in high biomass regions and reduces atmosphere influences (Huete *et al.*, 2002).
Leaf Water Content Index	$LWCI = \frac{-log[1 - (\rho_{830} - \rho_{1650})]}{-log[1 - (\rho^{FT}_{830} - \rho^{FT}_{1650})]}$	Detects the water stress and determines the Relative Water Content in plants (Hunt and Rock, 1989). The values, $\rho^{\text{FT}}_{830} = 0.859$ and $\rho^{\text{FT}}_{1650} = 0.262$, were calculated according to the non-stressed leaf reflectances, see Table 1 in (Hunt *et al.*, 1987).
Moisture Stress Index	$MSI = \frac{\rho_{1650}}{\rho_{1260}}$, $MSI = \frac{\rho_{1600}}{\rho_{820}}$	Provide an indication of relative leaf/canopy moisture, see (Rock *et al.*, 1985, Hunt and Rock, 1989).
Normalized Difference Infrared Index	$NDII = \frac{\rho_{850} - \rho_{1650}}{\rho_{850} + \rho_{1650}}$	Estimate the moisture content in the root zone of vegetation (Sriwongsitanon *et al.*, 2016).
Normalized Difference Moisture Index	$NDMI = \frac{\rho_{1650} - \rho_{830}}{\rho_{1650} - \rho_{850}}$	Canopy water content. It was utilized in detection of forest disturbances (Jin and Sader, 2005).
Normalized Difference Mud Index	$NDMudl = \frac{\rho_{795} - \rho_{990}}{\rho_{795} + \rho_{990}}$	Muddy or very shallow water (Bernstein *et al.*, 2012).
Normalized Pigment Chlorophyll Ratio Index	$NPCI = \frac{\rho_{680} - \rho_{430}}{\rho_{680} + \rho_{430}}$	Ratio between total pigments and chlorophyll *a*. This ratio decrease in healthy and rise in stressed or senescing aquatic vegetation (Peñuelas *et al.*, 1993, 1994).
Normalized Difference Vegetation Index	$NDVI = \frac{\rho_{830} - \rho_{660}}{\rho_{830} + \rho_{660}}$, $NDVI = \frac{\rho_{900} - \rho_{680}}{\rho_{900} + \rho_{680}}$	Green biomass, Leaf Area Index, Vegetation (Ionue *et al.*, 2008, Peñuelas *et al.*, 1995).
Normalized Difference Water Index	$NDWI = \frac{\rho_{860} - \rho_{1240}}{\rho_{860} + \rho_{1240}}$	Soil/vegetation water content from space (Gao, 1996).
Normalized Multi-band Drought Index	$NDMI = \frac{\rho_{860} - (\rho_{1640} - \rho_{2130})}{\rho_{860} + (\rho_{1640} - \rho_{2130})}$	Soil/vegetation water content from space (Wang and Qu, 2007).
Normalized Phaeophytinization Index	$NPQI = \frac{\rho_{415} - \rho_{435}}{\rho_{415} + \rho_{435}}$	Chlorophyll degradation. It is sensitive to mite attack effects on apple trees (Peñuelas *et al.*, 1995).
Photochemical Reflectance Index	$PRI = \frac{\rho_{531} - \rho_{570}}{\rho_{531} + \rho_{570}}$	Photosynthetic radiation use efficiency of plant leaves (Ionue *et al.*, 2008).
Shortwave Infrared Water Stress Index	$SIWSI = \frac{\rho_{1640} - \rho_{860}}{\rho_{1640} + \rho_{860}}$, $SIWSI = \frac{\rho_{1240} - \rho_{860}}{\rho_{1240} + \rho_{860}}$	Soil/Canopy water content (Fensholt and Sandholt, 2003).
Simple Ratio Pigment Index	$SRPI = \frac{\rho_{430}}{\rho_{680}}$	Ratio between carotenoid and chlorophyll a concentrations (Car/Chl*a*).
Soil-Adjusted Vegetation Index	$SAVI = \frac{1.5\ (\rho_{830} - \rho_{660})}{\rho_{830} + \rho_{660} + 0.5}$	Vegetation, minimizing soil-induced variations (Huete, 1988, Ionue *et al.*, 2008).
Structure Insensitive Pigment Index	$SIPI = \frac{\rho_{800} - \rho_{445}}{\rho_{800} + \rho_{680}}$	Ratio between carotenoid and chlorophyll *a* concentrations (Car/Chl*a*). This ratio characterizes the physiology and phenology of vegetation (Peñuelas *et al.*, 1995b).
Water Band Index	$WBI = \frac{\rho_{970}}{\rho_{900}}$	Plant Water Concentration (Peñuelas *et al.*, 1994). It is the reciprocal of WI.
Water Index	$WI = \frac{\rho_{900}}{\rho_{970}}$	Plant Water Concentration (Peñuelas *et al.*, 1997).

Table 4. Sets of functions and terminals utilized by BP to create $\text{EVO}_{\text{spectral}}$.

$F_{\text{spectral}} =$	$\{+, -, \times, \div, \lvert\cdot\rvert, \lvert+\rvert, \lvert-\rvert, \sqrt{}, ()^2, ln(), +k, -k, \times k, \div k, \sqrt[k]{}, ()^k, infimum(), supremum(), \text{NDSI}()\}$
$T_{\text{spectral}} =$	$H_I \cup \{\text{ARV I, EV I, LWCI, MSI, NDII, NDMI, NDMudI, NPCI, NDVI, NDWI, NMDI, NPQI, PRI, SIWSI, SRPI, SAV I, SIPI, WBI, WI}\}$

mentioned in Section 2.3.1, MM is an important ally to extract structural information from images.

Fundamental morphological operators utilize a Structuring Element (SE) for scanning the image and investigate the morphological properties of the structures contained in the image, e.g., highlighting the structures with similar shape and size to the SE. In general, a SE is the elementary *n*-dimension neighborhood zone centered at pixel x, known as origin, and $\Psi_B(f)$ is the morphological transformation Ψ of image *f* using *B* as an SE. The origin allows the positioning of the SE at every pixel in the image. Usually, a SE is a two-dimensional neighborhood of binary values, in which the true pixels characterize the shape of the SEs. Given their image values independence, 2D SEs can be used with H_Is. Figure 4 illustrates the six elementary shapes of *flat* SEs utilized by morphological operations. Furthermore, each SE shape has different size, and orientation when applies. Specifically, disk, square, and line shapes were used to create SEs with three neighborhood

Table 5. Morphological operators with their corresponding brief description.

Morphological Functions	Formula	Description
Erosion	$\varepsilon_B(f) = \wedge_{b \in B} f_{-b}$	Erosion of a grayscale image f using a structuring element B is defined as the minimum of the translations of f by the vectors **-b** in B. To put it another way, the eroded value of a pixel x is the minimum value of the image in the neighborhood defined by the SE when its origin is at x.
Dilation	$\delta_B(f) = \vee_{b \in B} f_{-b}$	Dilation of a grayscale image f using a structuring element B is defined as the maximum of the translations of f by the vectors **-b** in B. In other words, the dilated value at a given pixel x is the maximum value of the image in the window defined by the SE when its origin is at x.
Opening	$\gamma_B(f) = \delta_{B'}[\varepsilon_B(f)]$	Opening (γ) of the grayscale image f is defined as the result of erosion by a structuring element B followed by the dilation with the reflected B'. Thus, γeliminates peaks that are smaller than the SE.
Closing	$\phi_B(f) = \varepsilon_{B'}[\delta_B(f)]$	Closing (ϕ) of the grayscale image f is defined as the result of dilation by a structuring element B followed by the erosion with the reflected B'. Hence, ϕ fills valleys that are smaller than the SE.
White top-hat	$WTH_B(f) = f - \gamma_B(f)$	White top-hat (WTH) of a grayscale image f is defined as the difference between the original grayscale image f and its opening γ.
Black tot-hat	$BTH_B(f) = \phi_B(f) - f$	Black top-hat (BTH) of a grayscale image f is defined as the difference between the closing ϕ of the original image and the original image.
Watershed transform	Algorithm	The basic notions of watershed transform was first introduced by Beucher and Lantuejoul, see (Beucher and Lantuejoul, 1979), and it's an algorithm for segmenting images, for more details about watershed transform, see (Meyer and Beucher, 1990). In this work, we utilize the algorithm proposed by Meyer (1993).

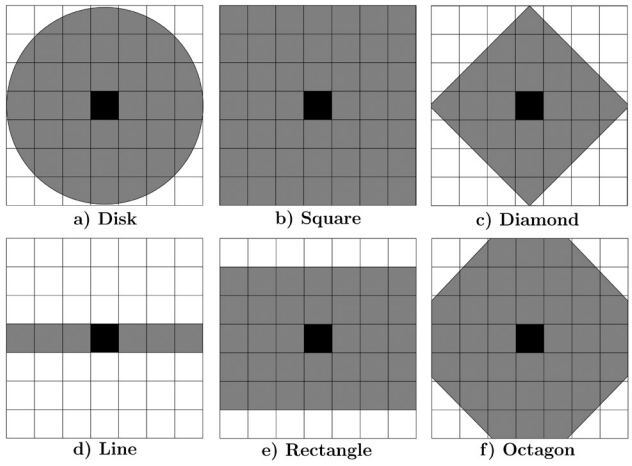

Figure 4. Structuring elements that will be used during evolution. Only SEs with 7 × 7 neighborhood are shown; the darker pixel is the origin pixel x, and the gray area indicates the shape of the SE.

sizes: 3×3, 5×5, and 7×7 pixels. The 3×3 and 5×5 diamond and octagon SEs are equal to 3×3 and 5×5 disk SEs, thus we utilized only the 7×7 size for diamond and octagon SEs. Also, the neighborhood size of rectangle SE is restricted to 3×5 and 5×7 pixels, because 1×3 neighborhood is the same as a line of size 3 and 0° of orientation. In addition to size, line shape SEs have three orientations, 0°, 45°, and 90°.

The fundamental operators in MM are erosion (ε) and dilation (δ) because all other morphological operators can be expressed in terms of them. A SE is used for inspecting the image, as a result, the application of erosion/dilation operator gives an eroded/dilated image which shows the locus of points where the SE fits/hits the objects in the image. For this reason, the shape and size of the SE is usually chosen according to the geometric properties of the relevant and irrelevant image structures (Soille, 2003). Rotationally symmetric SEs are often employed for the opening transformations because the results do not depend on the orientation of the image.

Soille and Pesaresi (2002) showed an analysis of the suitability of MM processing for earth observation imagery. Also, morphological processing provides a good, simplified approach to perform joint spatial/spectral classification of urban hyperspectral data (Plaza *et al.*, 2009). Regarding the desirability of using MM for the extraction of spatial features from H_Is, see (Sternberg, 1986). Table 5 shows some morphological operators used in geoscience and remote sensing applications. For a formal and more detailed explanation of each MM operators, see Soille (2003).

In summary, 1,719 bands that constitute an H_I compound the $T_{spatial}$ set. Whereas that, the set $F_{spatial}$ of functions is compounded by the morphological operators in Table 6.

Note that each operator can be used together with any of the SEs described above, this is nineteen different SEs, resulting in a total of 116 morphological operators. Additionally, we added arithmetic functions to allow the BP algorithm to establish relationships among morphological operators. Table 6 shows the set of functions and terminals of $EVO_{spatial}$.

Fitness Function and Accuracy Evaluation

The features selection problem involves the selection of a subset of d features from a total of D features, based on a given optimization criterion $F(X)$, where X denotes the subset of selected features (Oh *et al.*, 2004).

In hyperspectral imaging literature, the feature selection problem is commonly known as band selection. Band selection consists in reducing the dimensionality of hyperspectral images and finding the useful wavelengths and spectral indices for analysis, classification and regression (Yoon and Park, 2015). In this study, F is represented by the fitness function used to assess X. The objective is to find a subset, X, that yields the highest accuracy rate of graves classification. Graves detection problem leads to unconstrained combinatorial optimization in which the classification accuracy is the search criterion. Owing to the capability of evolutionary computation to efficiently search in large spaces, such important set of heuristic algorithms are well suited to approaching feature selection (Iglesia, 2013). In this aspect, evolutionary computation offers an alternative to the well-known Principal Components Analysis or Random Forest to deal with high dimension of hyperspectral data (Plaza *et al.*, 2009).

We can say that, each individual genotype represents an H-VAM, although we know that it only encodes the operators of extraction and integration of features. Each H-VAM is evaluated with a set of hyperspectral images, called training set, the resulting BSMs are compared against a ground truth map and the classification accuracy is calculated from these values. In this

Table 6. Sets of functions and terminals utilized by BP to create $EVO_{spatial}$.

$F_{spatial}$ =	$\{\varepsilon_B(), \delta_B(), \gamma_B(), \phi_B(), WTH(), BTH(), Watershed(), \sim Watershed(), +, -, \times, \div, \lvert\cdot\rvert, \lvert+\rvert, \lvert-\rvert, \sqrt{}, ()^2, ln(), +k, -k, \times k, \div k, \sqrt[k]{}, ()^k, infimum(), supremum()\}$
$T_{spatial}$ =	H_I

section, we explain how the accuracy of H-VAMs was evaluated; such an evaluation criterion is regarded as a fitness function.

The BSM shows the classification of each pixel in H_I made by a given H-VAM, where a 0 means "no grave" soil category, whereas a 1 indicates that there is a "grave". Note that accuracy measures are not processed directly from the raw classifier outputs. Instead, an error matrix, also known as confusion matrix, is used to quantify the accuracy of classification results (Congalton, 1991).

An error matrix can be used for many analytical statistical techniques. Among these techniques, the discrete multivariate techniques are of particular importance for the aim of this work because hyperspectral data are discrete rather than continuous and follow a multinomial distribution. Since Congalton *et al.* (1983) used discrete multivariate techniques for performing statistical test on the classification accuracy of digital remotely sensed data, these techniques have been adopted as the standard accuracy assessment tools (Congalton, 1991).

In this study, we use the Kappa coefficient of agreement (κ) (Equation 5) and weighted Kappa coefficient of agreement (κ_w) (Equation 6) as fitness function because κ statistic has been frequently used in analyses of error matrices (Stehman, 1996) and κ uses all the elements of the error matrix, and not just the diagonal elements, as is the case with overall accuracy (Varshney and Arora, 2004).

The κ coefficient is defined as follows:

$$\kappa = \frac{N\sum_{i=1}^{r} x_{ii} - \sum_{i=1}^{t}\left(x_{i+} * x_{+1}\right)}{N^2 - \sum_{i=1}^{t}\left(x_{i+} * x_{+1}\right)} \tag{5}$$

where r is the number of rows, which is also the number of classes, in the matrix, x_{ii} is the number of observations in row i and column i, x_{i+} and x_{+i} are the marginal totals of row i and column i, respectively, and N is the total number of observations (Congalton, 1991, Stehman, 1996).

The κ_w coefficient can be calculated as follows:

$$\kappa_w = \frac{\sum_{i=1}^{I}\sum_{j=1}^{I} w_{ij}P_{ij} \sum_{i=1}^{I}\sum_{j=1}^{I} w_{ij}P_iP_j}{1 - \sum_{i=1}^{I}\sum_{j=1}^{I} w_{ij}P_iP_j} \tag{6}$$

where w_{ij} denotes the weight the i^{th} row and j^{th} column of the table of weights, $w_{ij} > 0$. P_{ij} are the observed probabilities, P_i and P_j are the expected probabilities, and I are the possible ordinal values of a class, $I = 2$.

In order to assign a fitness value to every individual in the population, each H-VAM is evaluated using a training set of hyperspectral images. During the evaluation of one H-VAM, one error matrix and its respective accuracy coefficient are obtained by each one of the H_I in the training set. As a result we have nine values of accuracy, the fitness value for an individual is the average of such values. Next, the fitness function is calculated as follows:

$$F = \frac{1}{n}\sum_{j=1}^{n} f_j \tag{7}$$

where $n = 9$ is the number of H_I in the training set, and f is κ or κ_w coefficient.

The results obtained during this study are discussed below.

Experimental Results

For the experiments, we apply a four-fold cross-validation method; the set of the twelve hyperspectral images (see the previous Section), was randomly divided into four subsets. Furthermore, two experiments were carried out, one of them with κ and the other with κ_w.

Experiments with Kappa

Structural Analysis of Solutions

We picked the forty best solutions and determined how frequent the functions and terminals were used within them in order to identify which components are useful for classification and which are not. The functions and terminals in the $EVO_{spectral}$ and $EVO_{spatial}$ operators are counted only if their respective CMs are used by the EFI.

The experimental results about $EVO_{spectral}$, show that 18 solutions (45%) utilize ÷ in 31 occasions, follow by: $\lvert I\rvert$ was used 33 times by 14 solutions (35%); $()^2$ was used 27 times in 13 solutions (32.5%); $\lvert-\rvert$, NDSI and $()^k$ were used 24, 23, and 41 times, respectively, by 10 individuals (25%).

All functions in $F_{spectral}$ were utilized by at least, two best solutions. On the other hand, the terminals in $T_{spectral}$ are 1,719 wavelengths, conforming H_I, plus 22 spectral indexes, so only a small percentage was used by the forty best solutions. The most used reflectances were ρ_{515}, ρ_{612}, ρ_{860}, and ρ_{2285} in two solutions. Only three spectral index were used and are: WBI(ρ_{900}, ρ_{970}), WI(ρ_{900}; ρ_{970}), and EVI(ρ_{469}; ρ_{645}; ρ_{859}).

In the same way, we analyzed the $EVO_{spatial}$. $Erode_{Sqr\_7}$ function was the most used by 3 individuals in 6 occasions, followed by: $BottomHat_{Oct\_7}$, $Open_{Ln\_3\_45}$, $Open_{Ln\_7\_45}$, $Erode_{Dmnd\_7}$. Only 43 of the 130 functions in $F_{spatial}$, 33%, were utilized in at least, one solution. Regarding $EVO_{spatial}$ terminals, $T_{spatial}$, we can say that there was no significant difference in frequency among the terminals used. But we can observe that only 41 of the 1,719 terminals were used.

Finally, we reviewed the results for EFI. The most frequent F_{FI} function among solutions was $()^2$, 30 out of 40 (75%) solutions utilized it, followed by: $\lvert I\rvert$ with 26 (65%) next, ÷ and $\times k$ with a frequency of 21 and 20, respectively. The T_{FI} set is composed by the conspicuity maps, $CM_{spectral}$ and $CM_{spatial}$. The most requested CM was $CM_{spectral}$, 38 of the solutions (95%) utilized it in 206 occasions. $CM_{spatial}$ was used in 31 solutions (77.5%) 144 times. This means that the spectral information has been more useful than spatial to solve the problem during the BP process.

In the next section we go into the analysis of the effectiveness of the best solution during the training and testing stages.

Effectiveness of Solutions

The best solution was selected based, firstly, on the fitness obtained during the training and, second, on the one obtained during the testing. The most eligible individual had a value of $\kappa = 0.3621$ in training stage, and a value of $\kappa = 0.3047$ in testing stage and utilizes spectral and spatial information, see Table 7. It is based on ρ_{969}, ρ_{2368}, ρ_{1546}, ρ_{2216} and ρ_{1271} wavelengths. Figure 5 shows the error matrices obtained by the best individual applied to each one of the H_Is. Matrices are ordered by sampling date, from oldest to most recent one. Three of the images were evaluated during testing stage, see Figure 5 (a), (b), and (f), with bold captions. Below each matrix, the

Table 7. The best solution of experiment with Kappa as fitness function.

	Best Individual	Fit_{trai}	Fit_{tst}
$EVOs_{pectral}$:	$((\lvert(\lvert(\rho_{969} * 8.86) + \rho_{2368}\rvert * ln(\rho_{1546} * 1.02))^{4.46} * 8.86) + \rho_{969}\rvert * ln(ln(\rho_{2216}))) * \ln(\rho_{2216}))^{19.89}$	0.3621	0.3047
$EVO_{spatial}$:	$\phi_{Ln\_5\_45}(\gamma_{Ln\_7\_45}(\phi_{Ln\_5\_45}(\gamma_{Ln\_7\_45}(\phi_{Ln\_5\_45}(\phi_{Ln\_5\_45}(\phi_{Ln\_5\_45}(\varepsilon_{Dsk\_7}(\varepsilon_{Dsk\_7}(\rho_{1271}))))))))$		
EFI:	$\lvert(((CM_{spectral})^{1.35} / (((\lvert(CM_{spectral} / (((CM_{spectral} * (CM_{spatial} + CM_{spectral})) * CM_{spatial}) / 307.42)) + CM_{spatial}\rvert * 2.26) / 307.42)) * 2.95) + ((CM_{spatial} + CM_{spectral})^{1/2} * CM_{spatial})\rvert$		

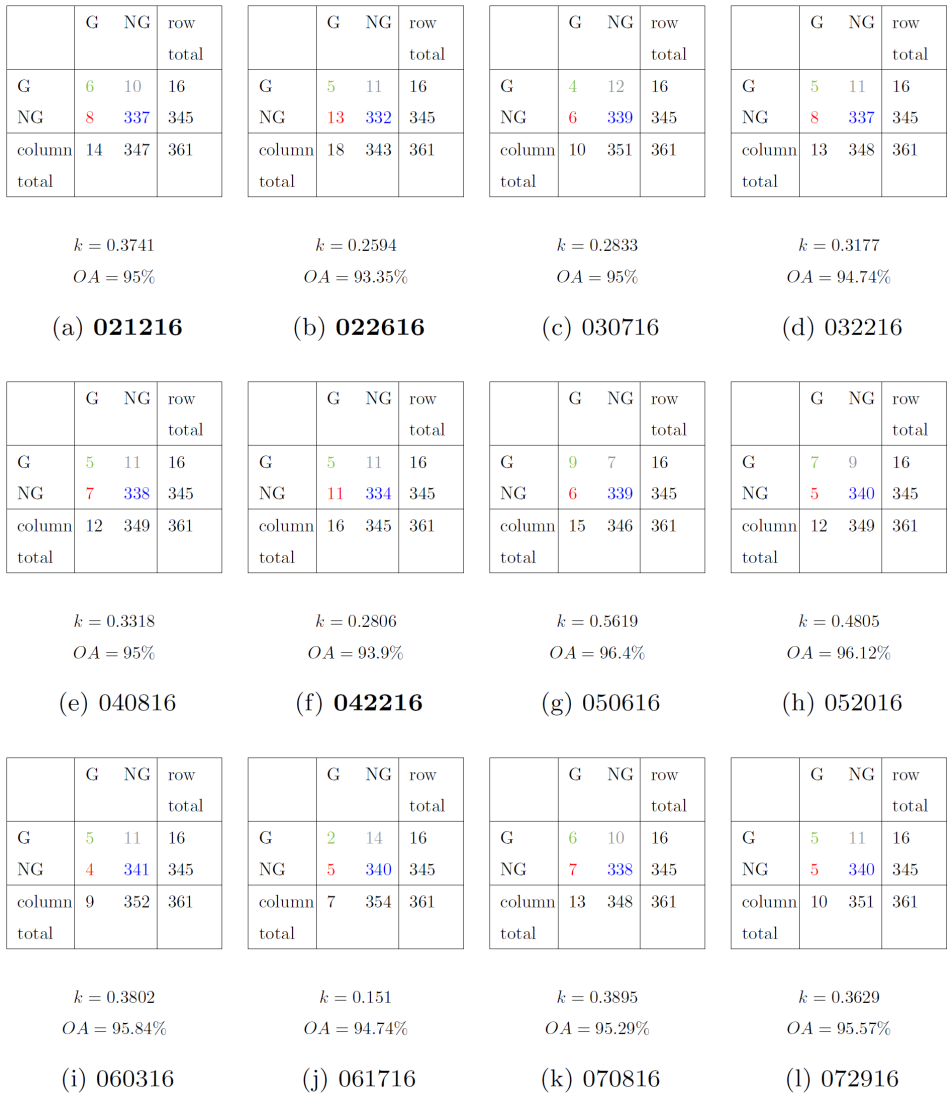

Figure 5. Error matrices for the twelve hyperspectral images, obtained by the best solution during Kappa experiments.

values of κ and of Overall Accuracy (OA) rate are shown. The best κ and OA classifications were made in the image 050616, with 96.4% and 052016 image, with 96.12%, (g) and (h) respectively, during May month. The worst accurate classifications were obtained in 022616 image, with 93.35%, and 042216 image, with 93.9%, (b) and (f) respectively, both from testing stage. The decreasing of performance is expected in testing stage. On the other hand, the text colors allow to relate the values of the error matrices with Figure 6.

Figure 6 depicts the spatial distribution of errors/successes detection for each image. These images are sorted according to the date they were taken, starting with the oldest and ending with the most recent. Regarding the pixel's color, green pixels indicate graves that were correctly classified as graves (true positives); gray pixels indicate graves that were incorrectly marked as no-graves (false negatives); red pixels indicate no-graves incorrectly classified as graves (false positives); blue pixels indicate no-graves correctly classified as no-graves (true negatives). These colors allow us to better analyze the classified images and infer information from the spatial arrangement of the results. For example, the pixel corresponding to the lower left corner of grave F4, see Figure 1 for graves labeling, was detected in ten of the twelve images. The most correctly detected grave was F2, it was fully detected in seven images and partially detected in one. Grave F6 was totally detected in three of the images. Finally, grave F7 was completely detected in one image and partially detected in three.

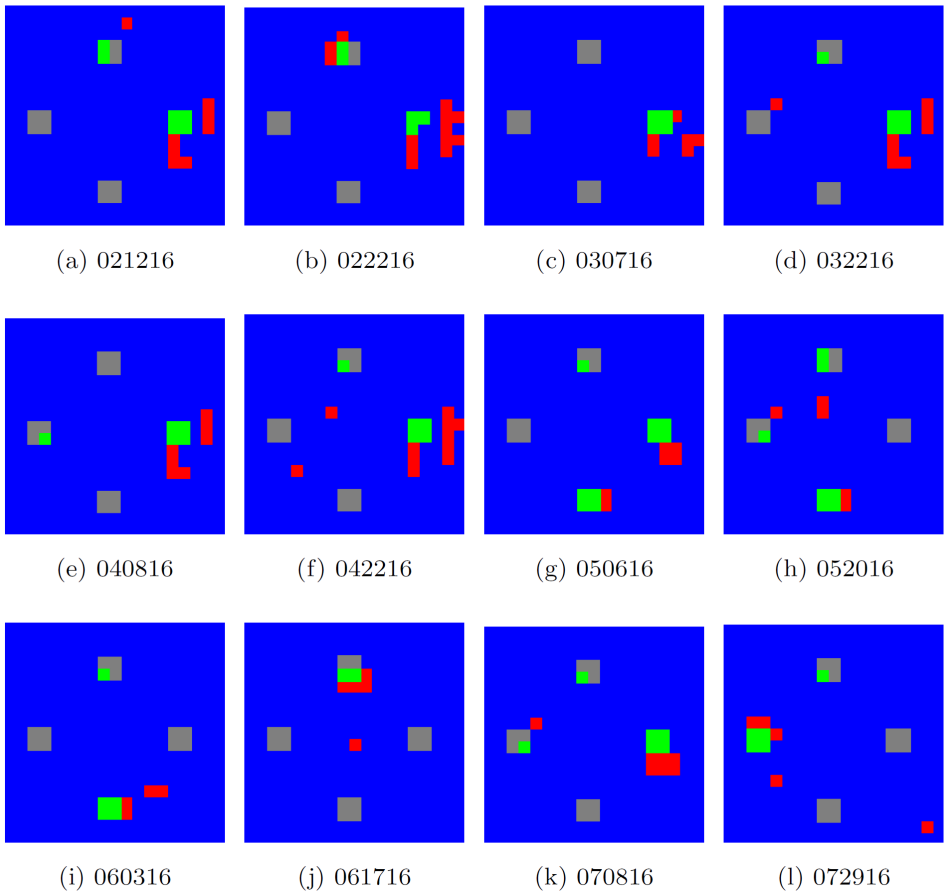

Figure 6. Binary saliency maps and classification of best individual over the twelve images.

We also analyzed the reflectance characteristics of the bands used by the best solution. We started with the bands used by $EVO_{spectral}$. First 969 nm (ρ_{969}), usually the 970 spectral region is used to estimate plant water concentration, e.g., water band index (WBI) and water index (WI), see Table 3. There is a water absorption peak near 970 nm (Danson *et al.*, 1992), so that the lower the leaf water content the higher reflectance is in the 970 nm region, because there is lower spectral absorption. In the same way, the band 1546 nm (ρ_{1546}) belongs to the Middle-Infrared spectral region (MIR, 1300-2500 nm), the interaction of vegetation with radiation in this region depends partly on the volume of water content in leaf cells. For this reason, the use of MIR wavelengths is suggested for remotely sensing leaf water contents, particularly from 1550 to 1750 nm (Tucker, 1980). Considering the reflectance characteristics at wavelength 2216 nm (ρ_{2216}), Olson and Zhu (1985) noted that the 2080 to 2350 nm band group (centered at 2215 nm) provides significant information about trees species, particularly near 2220 nm. Moreover, the bands around 2020 to 2220 nm are considered important for cellulose or lignin detection using remote sensing data as they are distinctive from soil minerals and less affected by atmospheric gases (Zandler *et al.*, 2015). The last wavelength used by the $EVO_{spectral}$ of the best solution is 2368 nm (ρ_{2368}), it has been said in (Herold, 2006) that the presence of calcium carbonates is suggested by features near 2330 nm, specifically for calcite (2300 nm) and dolomite (2370 nm). In this same sense, recently Roberts *et al.* (2013) discovered that natural surfaces, including organic matter and microbial biomass, possessing a high density of carboxyl groups may be a mechanism by which ordered dolomite nuclei form. With regard to $EVO_{spatial}$, it utilizes the 1271 nm wavelength (ρ_{1271}). This may be explained because the spatial information can be best extracted from a high-contrast band and the wavelength of 1271 nm falls within the NIR waveband, which is a spectral region of high contrast during early vegetation regrowth. According to Dehaan and Taylor (2002), Samphire (*Halosarcia pergranulata*), a dense succulent shrub, is characterized by having a distinctive slope to the infrared reflectance plateau between 1250 and 1400 nm, and the spectra of cultivated mixed rye and clover pasture vegetation, show a nearly at infrared reflectance high between 1250 and 1450 nm.

Experiments with Weighted-Kappa

In light of observations from the first experiment with Kappa coefficient as fitness function, we decided to do another experiment by changing the fitness function by the weighted Kappa (κ_w) statistic to try to improve the results. The approach of κ_w seems useful in two different situations: first, when categories of thematic maps are ordered. For ordered categories it can be easily recognized that relative disagreement may vary, even though κ_w was introduced in the title of the article by Cohen (1968) as a measure for 'nominal scale agreement'; second, when the categories are classified according to nominal or ordinal scales, and the seriousness of erroneous map data could be quantified for a certain map user or group of map users (Naesset, 2014). It is usually unrealistic to assume that all the errors are of identical importance because it is a human subjective decision.

In order to calculate κ_w is necessary to establish a table of weights which measure the degree of disagreement between

the two type of errors, false positive and false negative, the higher the disagreement the higher the weight. The table of weights should be a matrix with zeros in the main diagonal and positive values off the main diagonal. Table 8 provides the weights used in this experiment, which can be interpreted in the following way: the error of classifying a grave as no-grave is four times less desirable than the error of classifying a no-grave as grave. Hence the H-VAM will tend to find more graves at the cost of increasing false detections.

Table 8. Disagreement weight matrix used during experiment with weighted Kappa.

	G	NG
G	0	4
NG	1	0

Although there are techniques for assigning values to the weights of disagreement, as proposed by Cicchetti and Allison (1971), in this study we based the selection of values on results obtained from several trials with different weight matrices.

Another change that was introduced to the fitness function is the binarization method of the image. While in the first experiments a binarization with threshold equal to zero was used, during these experiments the method proposed by Otsu (1979) was used to determine the binarization threshold dynamically. Below, we show the analysis of the results of this second experiment using κ_w as fitness function.

Structural Analysis of Solutions

In this section we analyze the structure of the best forty solutions by calculating the use frequency of functions and terminals, with the aim of identifying which are the components that are useful for classification and which are not. The functions and terminals in the $EVO_{spectral}$ and $EVO_{spatial}$ operators are only counted if their respective CMs are used by the EFI.

First, we analyzed $EVO_{spectral}$ operator. Regarding $F_{spectral}$ set, 14 solutions (35%) used ÷ in 30 occasions, follow by the NDSI and $|I|$, used by 11 solutions (27.5%), in 20 and 31 occasions, respectively. The $|-|$ function was used by 8 solutions (20%) in 11 occasions, +, $()^k$ and *ln* were used by 6 solutions (15%) in 23, 40, and 17 occasions, respectively. This functions were also, the most utilized by the best solutions obtained in the experiments with κ. On the contrary, $+k$, × and *supremum* functions were the less used. Therefore, based on the results of both experiments, it is logical to think that ÷, $|I|$, $()^2$, and the NDSI are useful for grave classification. About the terminals set $T^{spectral}$, the most used wavelengths were ρ_{582}, ρ_{1650} and WBI (ρ_{900}, ρ_{970}) spectral index, 2 times by 2 best solutions; Interestingly, considering the big number (1741) of terminals, these last two terminals are also among the most used terminals in the κ experiments.

Following a similar procedure, we analyzed the $EVO_{spatial}$ operator. $Erode_{Dsk\_7}$ and $Erode_{Ln\_7\_0}$ were the most used functions in four best solutions, followed by: $Dilate_{Rct\_5\times7}$, $Erode_{Oct\_7}$ and $Erode_{Sqr\_5}$ in three solutions. Remember that erosion and dilation are the fundamental operators in MM. At the end, Only 60 of the 130 functions in $F_{spatial}$ (46.15%) were utilized in at least, one solution. Regarding $EVO_{spatial}$ terminals, $T_{spatial}$, ρ_{1292} was the most used wavelength in two solutions. In experiments with Kappa the ρ_{1290} was used by one best solution, and it is very near to ρ_{1292}. There is no difference in frequency among the remaining terminals that were used. But we can observe that only 42 of the 1719 terminals were used, very similar to results in experiments with κ.

Finally, we also analyzed the results for EFI. The most frequent F_{FI} function among solutions is $()^k$, 25 solutions utilized it (62.5%). Next, $|I|$ was used by 24 solutions (60%) followed by $()^2$ with 22 invocations (55%). The ÷, $|-|$, $|+|$ functions have a frequency of use of 18, 15, and 15 solutions, respectively. Note that $()^2$ function was the most used during κ experiments and $|I|$ was the second one. In addition, ÷ function is also among the most used in both experiments. The terminals, $CM_{spectral}$ and $CM_{spatial}$, have the same frequency value, this is 35 solutions (87.5%). In this respect, results of EFI are quite different from κ experiments being the use of CMs more balanced in this case. These results suggest that the κ_w allows the BP to more extensively explore spatial information space without neglecting the spectral information. There is a balance between the two.

In the next section we go into the analysis of the effectiveness of the best solution during the training and testing stages.

Effectiveness of Solutions

In the same way as with κ experiments, we have selected the best individual, shown in Table 9, it got an average value of $\kappa_w = 0.4285$ in the training stage and of $\kappa_w = 0.3662$ in the testing stage. This solution is based on spectral and spatial information and is based on ρ_{653}, ρ_{796}, ρ_{861}, ρ_{841}, and ρ_{2243} terminals. This solution has a peculiarity: most utilized wavelengths belong to the VNIR portion of the electromagnetic spectrum, except for ρ_{2243} that belongs to the SWIR2 portion. The error matrices generated by the best solution on the twelve images, are shown in Figure 7. Three of the images were evaluated during testing stage: 030716, 052016, and 060316, their error matrices are shown in Figure 7c, 7h, and 7i, respectively, with bold captions. Below each error matrix are shown the values of κ, κ_w, and OA rate. The best κ_w values were obtained in images 052016 with $\kappa_w = 0.5404$, $\kappa = 0.4719$ and OA=94.46% and in 070816 image with $\kappa_w = 0.4963$, $\kappa = 0.4001$ and OA=92.8%, both are shown in Figure 7h) and 7k). The worst accurate classifications were obtained in the 030716 image with $\kappa_w = 0.2052$, $\kappa = 0.1976$ and OA=92.8%, and in 060316 image with $\kappa_w = 0.3038$, $\kappa = 0.353$ and OA=92.52%, both are shown in Figure 7c and 7i.

In order to compare the performance of the best solution obtained with κ against the one obtained with κ_w, we calculated the average precision and recall of the classification of the twelve H_is, and Table 10 depicts the results.

Considering that the purpose of using κ_w was to guide evolution by penalizing more the classification of a "grave" as a "no-grave" than a "no-grave" as a "grave". The results shown in the Table 10 are consistent with that objective. Since penalizing one error more than the other, caused that the solutions tended to make the less penalized error without suffering a considerable decrease in its fitness, which in turn causes the decrease in its precision. But, by heavily penalizing the classification of a "grave" as a "no-grave", the recall improved considerably, relative to κ, which was what we were looking for when implementing κ_w, even at the cost of a lower accuracy.

Then, the average κ, precision, and recall measures, obtained by the best solutions of the κ and κ_w experiments were calculated for the first three months and for the last three months of the monitoring period, separately; see Table 11. These results suggest that, although some graves classification was possible in the images obtained during the first three months, the measures mentioned above improve notably in the images obtained after the three months. Figure 8 shows that, in the case of the best solution of κ_w experiment, the classification of graves F4 and F6, the ones with less buried carcasses, two and one, respectively, improves in images acquired after three months. It seems logical to think that the number of buried bodies is related with the optimal window of time for image acquisition.

On the other hand, Figure 8 depicts the spatial distribution of detection errors/successes in each image. The most detected

Table 9. The best solution of experiment with weighted Kappa as fitness function.

	Best Individual	Fit_{trai}	Fit_{tst}
$EVO_{spectral}$:	$NDSI(Inf((((\rho_{841} - \rho_{2243})^4 + ((\rho_{796})^{1/2} * 1.90)) - 1.95), (\rho_{841} - \rho_{2243})^4), \rho_{653})$	0.4285	0.3662
$EVO_{spatial}$:	$BTH_{Ln\_5\_45}(\varepsilon_{Sqr\_7}(\rho_{861})$		
EFI:	$Ln((\lvert CM_{spatial}+((CM_{spectral})^{1/3.91}*17.06)^2 \rvert - ((\lvert CM_{spatial}+(CM_{spatial})^2 \rvert - (CM_{spatial})^{1/3.91}) * 4.13)^{1/3.91}) * 4.13) * (CM_{spatial}+19.26)^{1/1.74}$		

	G	NG	row total
G	9	7	16
NG	16	329	345
column total	25	336	361

$k = 0.4070$
$k_w = 0.4728$
$OA = 93.63\%$

(a) 021216

	G	NG	row total
G	7	9	16
NG	14	331	345
column total	21	340	361

$k = 0.3454$
$k_w = 0.3777$
$OA = 93.63\%$

(b) 022616

	G	NG	row total
G	4	12	16
NG	14	331	345
column total	18	343	361

$k = 0.1976$
$k_w = 0.2052$
$OA = 92.8\%$

(c) **030716**

	G	NG	row total
G	7	9	16
NG	12	333	345
column total	19	342	361

$k = 0.3697$
$k_w = 0.3908$
$OA = 94.18\%$

(d) 032216

	G	NG	row total
G	7	9	16
NG	15	330	345
column total	22	339	361

$k = 0.3343$
$k_w = 0.3713$
$OA = 93.35\%$

(e) 040816

	G	NG	row total
G	8	8	16
NG	14	331	345
column total	22	339	361

$k = 0.3897$
$k_w = 0.4330$
$OA = 93.91\%$

(f) 042216

	G	NG	row total
G	8	8	16
NG	10	335	345
column total	18	343	361

$k = 0.4445$
$k_w = 0.4616$
$OA = 95.01\%$

(g) 050616

	G	NG	row total
G	10	6	16
NG	14	331	345
column total	24	337	361

$k = 0.4719$
$k_w = 0.5404$
$OA = 94.46\%$

(h) **052016**

	G	NG	row total
G	7	9	16
NG	18	327	345
column total	25	336	361

$k = 0.3038$
$k_w = 0.3530$
$OA = 92.52\%$

(i) **060316**

	G	NG	row total
G	9	7	16
NG	18	327	345
column total	27	354	361

$k = 0.3843$
$k_w = 0.4589$
$OA = 93.07\%$

(j) 061716

	G	NG	row total
G	10	6	16
NG	20	325	345
column total	30	331	361

$k = 0.4001$
$k_w = 0.4963$
$OA = 92.8\%$

(k) 070816

	G	NG	row total
G	8	8	16
NG	20	325	345
column total	28	333	361

$k = 0.3256$
$k = 0.3939$
$OA = 92.24\%$

(l) 072916

Figure 7. Error matrices for the twelve hyperspectral images obtained by the best solution during weighted Kappa experiments.

grave was F2 (see Figure 1 for graves labeling); it was fully detected in five images and partially detected in seven, at last one pixel of F2 was detected in all images. The grave F7 was the most fully detected in eleven images. These results are consistent with the number of carcasses in the graves F2 and F7, since they are the ones with the most buried bodies, i.e., three and four respectively. The grave F6 was totally detected in one image and partially detected in two. Finally, the grave F4 was fully detected in one image and partially detected in another.

We also analyzed the properties of reflectance at the bands used by the best solution. First, the bands used by $EVO_{spectral}$. Some studies link the use of spectral region near the 653 nm band (ρ_{653}) to high green biomass regions and to vegetation

Table 10. Average precision, recall and κ of the best solutions of κ, κ_w and PLS-VIP (Silván-Cárdenas et al., 2017) experiments.

	Average		
Experiment	Precision	Recall	κ
κ	0.4339	0.3333	0.3477
κ_w	0.3383	0.4896	0.3645
PLS-VIP	0.2416	0.2813	0.2086

indices as EVI and SAVI (Peñuelas *et al.*, 1995; Huete, 1988; Huete *et al.*, 2002; Ionue *et al.*, 2008). Considering the spectral characteristics of the band 796 nm, in (Peñuelas *et al.*, 1995) the authors used the ρ_{800} to characterize the physiology and phenology of a wide range of leaves species and conditions. Furthermore, ρ_{796} and ρ_{841} are in the NIR (700 to 900 nm) spectral region, NIR is only affected by leaf internal structure and leaf dry matter content but no by water content. A combination of SWIR and NIR reflectance information can remove the effect of leaf internal structure and leaf dry matter content and it can improve the accuracy of retrieving the vegetation water content (Fensholt and Sandholt, 2003). Regarding the ρ_{2243}, Sims and Gamon (2003) and Jin and Sader (2005) reported that the band centered at 2250 nm has water absorption features and it can be used for prediction of plant water status. Besides, as it had previously been seen in previous , there is significant information about trees species in spectral bands near 2220 nm (Olson and Zhu, 1985). With regard to $EVO_{spatial}$, it utilizes the 861 nm wavelength (ρ_{861}) that also belongs to NIR spectral region.

About the complexity of the solutions obtained by the BP, the operations that consume more time are the MM, $()^{1/2}$, $()^{1/k}$, $()^2$ and $()^k$, and multiplication and division of images ($\times$, $\div$). In this study the H_Is have a size of 19 x 19 pixels, so the execution time of a H-VAM algorithm in an H_I takes a fraction of a second in a computer Intel ®Core™ 5-6500 at 3.20GHz, and 7.7GB in RAM. The best H-VAMs are simple and utilize a small amount of computational resources and time.

Finally, a comparison among the results of the experiments with κ and κ_w, and the ones reported by Silván-Cárdenas *et al.* (2017) was conducted. In such study, the authors utilized a Partial Least Squares (PLS) method followed by a technique of variable selection, based on Variable Importance of Projection (VIP) method, called Bootstrap-VIP, to compute spectral separability for detection of graves. According to the study of Maitra and Yan (2008), the PLS technique is more efficient than the Principal Component Analysis (PCA) technique for dimension reduction due to the supervised nature of its algorithm. In light of this finding, it is not necessary to compare our results against those obtained through PCA. We obtained the error matrices from the images shown in Figure 8 in (Silván-Cárdenas *et al.*, 2017) in order to compute the average κ, precision and recall. The results of such computation are shown in Table 10. Our two evolutionary approaches were better than PLS-VIP approach regarding these three criteria. This may be explained by the limited capability of a linear mapping of spectral information through PLS, unlike the highly non-linear HVAMs that put spectral and spatial information together. The best precision was obtained by our approach guided by κ. The best recall and detection accuracy, measured with κ coefficient of agreement, were obtained by our evolutionary approach guided by κ_w. Thereby, the strategy of setting the κ_w as fitness function of the BP optimization algorithm gave the expected results, improving the detection accuracy of BP compared with κ and PLS-VIP

Table 11. Average precision, recall and κ, for the first and last three months, of the best solutions of κ and κ_w experiments.

	First three months average:			Last three months average:		
Experiment	Precision	Recall	κ	Precision	Recall	κ
κ	0.37	0.3125	0.3078	0.4977	0.3542	0.3877
κ_w	0.3276	0.4375	0.3406	0.3572	0.5417	0.3884

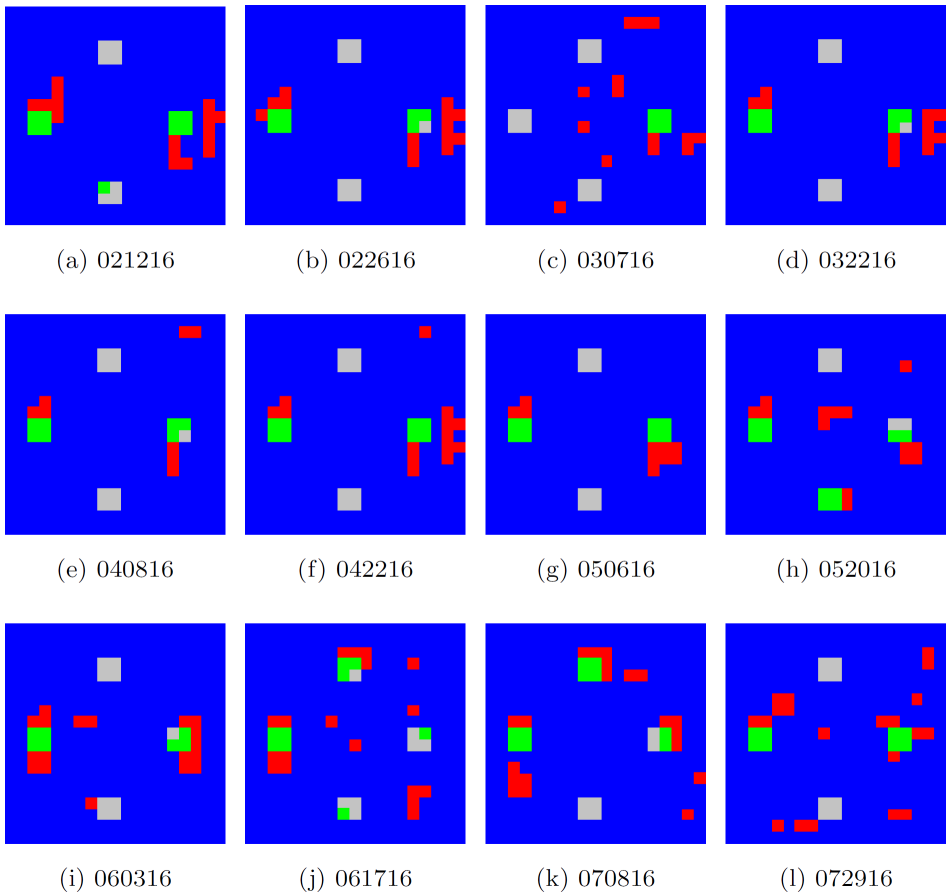

Figure 8. Binary saliency maps and classification of best individual obtained with weighted Kappa over the twelve images.

approaches. In addition, the results of our experiments show that the greater the use of spatial information, the performance of H-VAMs is better, so we can say that spatial information was crucial to improve the classification accuracy. This is an advantage over approaches such as PLS that only uses spectral information. Also, it should be noted that unlike PLS, the H-VAMs perform the classification of the image by themselves.

Conclusions

The objective of the present study was to assess the potential of utilizing a Brain Programming evolutionary strategy together with hyperspectral imagery for detecting clandestine graves. The method was tested with ground-based hyperspectral images of simulated graves containing pig cadavers and false empty graves.

The results in both experiments showed that ÷, NDSI, |I|, |−| and $()^k$ functions and the WBI spectral index are among the most utilized by the best solutions for extraction of spectral features. Regarding the extraction of spatial features, the most utilized morphological functions were: $Erode_{Sqr\_7}$, $Erode_{Dsk\_7}$ and $Erode_{Ln\_7\_0}$. The erode function is a simple and fundamental operator in mathematical morphology. Among the most used structuring elements are those of size 5 and 7 pixels.

In both experiments the spatial information was the most utilized throughout the evolution when using a weighted Kappa coefficient of agreement. This can be the reason of why H-VAMs of κ_w had a better detection accuracy.

As for the temporal window of optimal graves detection, we found that both experiments, the BP and H-VAM approach had a higher detection precision in the images acquired during the last three months than those acquired during the first three months. All this suggests that the best time for image acquisition is after three months. Although our approach detects some of the graves in the images acquired during the first three months.

After analyzing the most useful spectral bands for graves detection, we found that during both experiments these bands are related with the spectral reflectance, or absorption, response to: plant water concentration (ρ_{969}, WBI, WI) (Danson *et al.*, 1992), volume of water in leaf cells (ρ_{1546}) (Tucker, 1980), cellulose or lignin (ρ_{2216}) (Zandler *et al.*, 2015), dolomite (ρ_{2368}) (Herold, 2006), high green biomass (ρ_{653}) (Huete *et al.*, 2002), leaf internal structure and leaf dry matter (ρ_{796}, ρ_{841}, ρ_{861}) (Fensholt and Sandholt, 2003) and plant water status (ρ_{2243}) (Jin and Sader, 2005). Some of them had been utilized to obtain characteristic information about trees species (ρ_{2216}, ρ_{2243}) (Olson and Zhu, 1985); to discriminate the Samphire (*Halosarcia pergranulata*) from cultivated mixed rye and clover pasture (ρ_{1271}) (Dehaan and Taylor, 2002); and to characterize a wide range of leaves species (ρ_{796}) (Peñuelas *et al.*, 1995). There is a clear tendency, in the best solutions, to use spectral bands that respond to the vegetation and the water content of the plants. These results support the theory that the decomposition of buried corpses affects vegetation structure and soil composition, and that such effects can be used to detect clandestine graves.

The best H-VAM detected the whole F7 grave in eleven of the twelve hyperspectral images and detected the whole F2 grave in five images and partially in seven. Thus, at least one pixel of F2 grave was detected in all images. These graves had the major number of buried carcasses, four and three, respectively. The classification accuracy decreases drastically in the F6 and F4 graves. These results indicate that the number of buried bodies plays an important role for detection. The inclusion of empty graves (F1, F3, and F5) allowed to test our method under a worst-case scenario and, therefore, reported detection accuracies can only be higher under a more ideal scenario, that is when no soil disturbance other than burial are present.

The best H-VAM algorithms found by the BP showed to be simple and fast. In fact, the H-VAM with the best accuracy is the simplest and fastest of the two.

The research around the detection of clandestine graves through hyperspectral images began recently. For this reason, all the information provided by the few researches on this subject is of great importance for future research in hyperspectral imagery, remote sensing, and other areas as forensic geology. In further work, it is possible to incorporate the information gathered in this and other research to accelerate the evolution process and to create new, more efficient hyperspectral models of attention aiming graves detection. With this goal in mind, more research should be done to create graves detectors in different scenarios, since the environment where burials take place may have very different characteristics. The incorporation of these characteristics into the method could improve their accuracy.

BP and H-VAMs can be used in any hyperspectral image classification problem e.g., urban soil classification, vegetation classification. In addition, the H-VAMs can be modified based on the *a priori* knowledge we have of the problem and thus adapt it to extract the necessary characteristics to solve it. On the other hand, there is great difficulty in obtaining a large amount of hyperspectral images that better reflect the enormous variety of soils and vegetation in which the graves can be found. This small number of images can lead to the BP overfitting the H-VAMs and its accuracy decreasing in the presence of any change in the characteristics of the scenario. In this sense, another disadvantage is that if we increase the number of images of the training set and the size of those images, the execution time of the BP can be increased to the order of weeks. Although the obtained H-VAMs would be more robust to changes in the environment.

Among the contributions of this work, we enlisted the following. First, the resulting H-VAMs for graves detection performed better compared with previous work. Second, the BP allows the automatic design of visual attention models for hyperspectral images; this helps researchers to solve the problem of moving from the classic model of visual attention to the hyperspectral model by hand. Third, a comparison of the results of using the κ and κ_w coefficients demonstrated that guiding the search of H-VAMs with κ_w yields better accuracy results due to the introduction of the degree of disagreement. And finally, the fourth, a new VAM, called H-VAM, for the fusion of spatial and spectral features of hyperspectral images is proposed as the base of task-specific evolved VAMs.

Acknowledgments

This research and data used in this paper was acquired thanks to the support provided by the institutional funds (FOINS) of the Mexican National Science and Technology Council (CONACyT), Grant No. 249205 "Viabilidad de las imágenes híperespectrales para la detección de fosas clandestinas en México". In addition, the authors acknowledge the valuable comments of the anonymous reviewers and editors of *PE&RS*.

References

Agnelli, D.A., A. Bollini, and L. Lombardi, 2002. Image classification: An evolutionary approach, *Pattern Recognition Letters*, 23:303–309.

Albarracín, J.F.H., J.A. d. Santos, and R. d. S. Torres, 2016. Learning to combine spectral indices with genetic programming, *Proceedings of the 29th SIBGRAPI Conference on Graphics, Patterns and Images (SIBGRAPI)*, Sao Paulo, Brazil, 408–415.

Awuley, A., and B.J. Ross, 2016. Feature selection and classification using age layered population structure genetic programming, *Proceedings of the IEEE Congress on Evolutionary Computation (IEEE CEC 2016)*, Vancouver, Canada.

Banzhaf, W., P. Nordin, R.E. Keller, and F.D. Francone, 1998. *Genetic Programming: An Introduction*, Morgan Kauffman Publishers, San Francisco, California.

Benediktsson, J.A., M. Pasaresi, and K. Arnason, 2003. Classification and feature extraction for remote sensing images from urban areas based on morphological transformations, *IEEE Transactions on Geoscience and Remote Sensing*, 41:1940–1949.

Bernstein, L.S.,X. Jin, B. Gregor, and S.M. Adler-Golden, 2012. Quick atmospheric correction code: Algorithm description and recent upgrades, *Optical Engineering*, 51(11):111719-1–111719-11.

Beucher, S., and C. Lantuéjoul, 1979. Use of watersheds in contour detection, *Proceedings of the Workshop on Image Processing*, CCETT/IRISA, Rennes, France, 2.1–2.12.

Borji, A., and L. Itti, 2013. State-of-the-art in visual attention modeling, *IEEE Transactions on Pattern Analysis and Machine Intelligence*, 35(1):185–207.

Caccianiaga, M., S. Bottacin, and C. Cattaneo, 2012. Vegetation dynamics as a tool for detecting clandestine graves, *Journal of Forensic Science*, 57(4):983–988.

Cao, Y., J. Zhang, Q. Tian, L. Zhuo, and Q. Zhou, 2015. Salient target detection in hyperspectral images using spectral saliency, *China Signal and Information Processing*, 1086–1090.

Chion, C., J.-A. Landry, and L.D. Costa, 2008. A genetic-programming-based method for hyperspectral data information extraction: agricultural applications, *IEEE Transactions on Geoscience and Remote Sensing*, 46(8):2446–2457.

Cicchetti, D.V., and T. Allison, 1971. A new procedure for assessing reliability of scoring EEG sleep recordings, *American Journal of EEG Technology*, 11:101–109.

Cohen, J., 1968. Weighted kappa: Nominal scale agreement with provision for scaled disagreement or partial credit, *Psychological Bulletin*, 70:213–220.

Congalton, R.G., R.G. Oderwald, and R.A. Mead, 1983. Assessing Landsat classification accuracy using discrete multivariate analysis statistical techniques, *Photogrammetric Engineering & Remote Sensing*, 49:1671–1678.

Congalton, R.G., 1991. A review of assessing the accuracy of classifications of remotely sensed data, *Remote Sensing of Environment*, 37:35–46.

Danson, F.M., M.D. Steven, T.J. Malthus, and J.A. Clark, 1992. High-spectral resolution data for determining leaf water content, *International Journal of Remote Sensing*, 13(3):461–470.

Davis, R.A., A.J. Charlton, S. Oehlschlager, and J.C. Wilson, 2006. Novel feature selection method for genetic programming using metabolomic HNMR data, *Chemometrics and Intelligent Laboratory Systems*, 81:50–59.

Dehaan, R.L., and G.R. Taylor, 2002. Field-derived spectra of salinized soils and vegetation as indicators of irrigation-induced soil salinization, *Remote Sensing of Environment*, 80:406–417.

Dozal, L., G. Olague, E. Clemente, and D.E. Hernández, 2014. Brain programming for the evolution of an artificial dorsal stream, *Cognitive Computing*, 6:528.

Fensholt, R., and I. Sandholt, 2003. Derivation of a shortwave infrared water stress index from MODIS near and shortwave infrared data in a semiarid environment, *Remote Sensing of Environment*, 87:111–121.

Gao, B.-C., 1996. NDWI - A normalized difference water index for remote sensing of vegetation liquid water from space, *Remote Sensing of Environment*, 58:257–266.

Herold, M., S. Schiefer, P. Hostert, and D.A. Roberts, 2006. Applying imaging spectrometry in urban areas, *Urban Remote Sensing*, (Qihao Weng, and Dale A. Quattrochi, editors), pp 137–161.

Huete, A.R., 1988. A soil-adjusted vegetation index (SAVI), *Remote Sensing of Environment*, 25:295–309.

Huete, A.R., K. Didan, T. Miura, E.P. Rodriguez, X. Gao, and L.G. Ferreira, 2002. Overview of the radiometric and biophysical performance of the MODIS vegetation indices, *Remote Sensing of Environment*, 83:195–213.

Hunt, E.R., Jr., B.N. Rock, and P.S. Nobel, 1987. Measurement of leaf relative water content by infrared reflectance, *Remote Sensing of Environment*, 22:429–435.

Hunt, E.R., and B.N. Rock, Jr., 1989. Detection of changes in leaf water content using near- and middle infrared reflectances, *Remote Sensing of Environment*, 30:43–54.

Iglesia, B., 2013. Evolutionary computation for feature selection in classification problems, *WIREs Data Mining Knowledge and Discovery*, 3:381–407.

Ionue, Y., J. Peñuelas, A. Miyata, and M. Mano, 2008. Normalized difference spectral indices for estimating photosynthetic efficiency and capacity at a canopy scale derived from hyperspectral and CO2 flux measurements in rice, *Remote Sensing of Environment*, 112:156–172.

Itti, L., C. Koch, and E. Niebur, 1998. A model of saliency-based visual attention for rapid scene analysis, *IEEE Transactions on Pattern Analysis and Machine Intelligence*, 20(11):1254–1259.

Jin, S., and S.A. Sader, 2005. Comparison of time series tasseled cap wetness and the normalized difference moisture index in detecting forest disturbance, *Remote Sensing of Environment*, 94:364–372.

Kalacska, M.E., and L.S. Bell, 2006. Remote sensing as a tool for the detection of clandestine mass graves, *Canadian Society of Forensic Science Journal*, 39(1):1–13.

Kalacska, M.E., L.S. Bell, A.G. Sanchez-Azofeifa, and T. Caelli, 2009. The application of remote sensing for detecting mass graves: An experimental animal case study from Costa Rica, *Journal of Forensic Sciences*, 54(1):159–166.

Kaufman, Y.J., and D. Tanré, 1992. Atmospherically Resistant Vegetation Index (ARVI) for EOS-MODIS, *IEEE Transactions on Geoscience and Remote Sensing*, 30(2):261–270.

Kawamura, K., N. Watanabe, S. Sakanoue, H. -J. Lee, Y. Inoue, and S. Odagawa, 2010. Testing genetic algorithm as a tool to select relevant wavebands from field hyperspectral data for estimating pasture mass and quality in a mixed sown pasture using partial least squares regression, *Grassland Science*, 56:205–216.

Khanna, S., A. Palacios-Orueta, M.L. Whiting, S.L. Ustin, D. Riaño, and J. Litago, 2007. Development of angle indexes for soil moisture estimation, dry matter detection and land-cover discrimination, *Remote Sensing of Environment*, 109:154–165.

Koza, J.R., 1992. *Genetic Programming: On the Programming of Computers by Means of Natural Selection*, Cambridge, Massachuttes, MIT Press.

Koza, J.R., 2010. Human-competitive results produced by genetic programming, *Genetic Programming and Evolvable Machines*, 11(3-4):251–284.

Landgrebe, D., 1999. Some fundamentals and methods for hyperspectral image data analysis, *Proceedings of The International Society for Optical Engineering (SPIE): Systems and Technologies for Clinical Diagnostics and Drug Discovery II*, San Jose, California. 3603:104–113.

Landry, J.-A., L. Da Costa, and T. Bernier, 2006. Discriminant feature selection by genetic programming: Towards a domain independent multi-class object detection system, *Journal of Systemics, Cybernetics and Informatics*, 3(1):76–81.

Leblanc, G., M. Kalacska, and R. Soffer, 2014. Detection of single graves by airborne hyperspectral imaging, *Forensic Science International*, 245:17–23.

Le Moan, S., A. Mansouri, J.Y. Hardeberg, and Y. Voisin, 2011. Saliency in spectral images, *Image Analysis* (A. Heyden, and F. Kahl, editors) *Image Analysis* (SCIA).

Le Moan, S., A. Mansouri, J.Y. Hardeberg, and Y. Voisin, 2013. Saliency for spectral image analysis, *IEEE Journal of Selected Topics in Applied Earth Observations and Remote Sensing*, IEEE, 1–8.

Li, S., H. Wu, D. Wan, and J. Zhu, 2011. An effective feature selection method for hyperspectral image classification based on genetic algorithm and support vector machine, *Knowledge-Based Systems*, 24:40–48.

Li, S., J. Qiu, X. Yang, H. Liu, D. Wan, and Y. Zhu, 2014. A novel approach to hyperspectral band selection based on spectral shape similarity analysis and fast branch and bound search, *Engineering Applications of Artificial Intelligence*, 27:241–250.

Liang, J., J. Zhou, X. Bai, and Y. Qian, 2013. Salient object detection in hyperspectral imagery, *Proceedings of the 20th IEEE Conference on Image Processing (ICIP).*

Maitra, S., and J. Yan, 2008. Two dimension reduction techniques for regression, *Principal Component Analysis and Partial Least Squares*.

Meyer, F., and S. Beucher, 1990. Morphological segmentation, *Journal of Visual Communication and Image Representation*, 1(1):21–46.

Meyer, F., 1993. Topographic distance and watershed lines, *Signal Processing*, 38:113–125.

Naesset, E., 2014. Use of the weighted Kappa coefficient in classification error assessment of thematic maps, *International Journal of Geographical Information Systems*, 10(5):591–603.

Noyel, G., J. Angulo, and D. Jeulin, 2007. Morphological segmentation of hyperspectral images, *Image Analysis & Stereology,* 26:101–109.

Oh, I. -S., J. -S. Lee, and B. -R. Moon, 2004. Hybrid genetic algorithms for feature selection, *Transactions on Pattern Analysis and Machine Intelligence*, 26(11):1424–1437.

Olson, C.E., and Z. Zhu, 1985. Forest species identification with high spectral resolution data, *IEEE Transactions on Systems, Man, and Cybernetics*.

Otsu, N., 1979. A threshold selection method from gray-level histograms, *IEEE Transactions on Systems, Man, and Cybernetics*, 9(1):62–66.

Peñuelas, J., J.A. Gamon, K.L. Griffin, and C.B. Field, 1993. Assessing community type, plant biomass, pigment composition, and photosynthetic efficiency of aquatic vegetation from spectral reflectance, *Remote Sensing of Environment*, 46:110–118.

Peñuelas, J., J.A. Gamon, A.L. Fredeen, J. Merino, and C.B. Field, 1994. Reflectance indices associated with physiological changes in nitrogen- and water-limited sunflower leaves, Remote Sensing of Environment, 48:135–146.

Peñuelas, J., I. Filella, P. Lloret, F. Mñnoz, and M. Vilajeliu, 1995. Reflectance assessment of mite effects on apple trees, *International Journal of Remote Sensing*, 16(14):2727–2733.

Peñuelas, J., F. Baret, and I. Filella, 1995. Semi-empirical indices to assess carotenoids/chlorophyll a ratio from leaf spectral reflectance, *Photosynthetica*, 31(2):221–230.

Peñuelas, J., J. Pinol, R. Ogaya, and I. Filella, 1997. Estimation of plant water concentration by the reflectance water index WI (R900/R970), *International Journal of Remote Sensing*, 18(13):2869–2875.

Pesaresi, M., and J.A. Benediktsson, 2001. A new approach for the morphological segmentation of high-resolution satellite imagery, *IEEE Transactions on Geoscience and Remote Sensing*, 39(2):309–320.

Plaza, A., J.A. Benediktsson, J.W. Boardman, J. Brazile, L. Bruzzone, G. Camps-Valls, J.

Chanussot, M. Fauvel, P. Gamba, A. Gualtieri, M. Marconcini, J.C. Tilton, and G. Trianni, 2009. Recent advances in techniques for hyperspectral image processing, *Remote Sensing of Environment*, 113:110–122.

Puente, C., G. Olague, S.V. Smith, H. Bullok, A. Hinojosa-Corona, and M.A. González-Botello, 2011. A genetic programming approach to estimate vegetation cover in the context of soil erosion assessment, *Photogrammetric Engineering & Remote Sensing*, 77(4):363–376.

Roberts, J.A., P.A. Kenward, D.A. Fowle, R.H. Goldstein, L.A. González, and D.S. Moore, 2013. Surface chemistry allows for abiotic precipitation of dolomite at low temperature, *Proceedings of the National Academy of Sciences*, 110(36):14540–14545.

Rock, B.N., D.L. Williams, and J.E. Vogelmann, 1985. Field and airborne spectral characterization of suspected acid deposition damage in red spruce (*picea rubens*) from Vermont, *Proceedings of the Machine Processing of Remotely Sensed Data Symposium*, Purdue University, West Lafayette, Indiana, 71–81.

Ross, B.J., A.G. Gualtieri, F. Fueten, and P. Budkewitsch, 2005. Hyperspectral image analysis using genetic programming, *Applied Soft Computing*, 5(2):147–156.

Sims, D.A., and J.A. Gamon, 2003. Estimation of vegetation water content and photosynthetic tissue area from spectral reflectance: A comparison of indices based on liquid water and chlorophyll absorption features, *Remote Sensing of Environment*, 84(4):526–537.

Siegel, J., and P. Saukko, 2013. *Encyclopedia of Forensic Sciences*, Academic Press.

Silván-Cárdenas, J.L., N. Corona-Romero, J.M. Madrigal-Gómez, A. Saavedra-Guerrero, T. Cortés-Villafranco, and E. Coronado-Juárez, 2017. On the detectability of buried remains with hyperspectral measurements, (J. Carrasco-Ochoa, J. Martínez-Trinidad J. Olvera-López, editors), *Pattern Recognition*, MCPR 2017. *Lecture Notes in Computer Science*, Vol 10267. Springer, Cham, Switzerland.

Smith, M.G., and L. Bull, 2005. Genetic programming with a genetic algorithm for feature construction and selection, *Genetic Programming and Evolvable Machines*, 6(3):265–281.

Soille, P., and M. Pesaresi, 2002. Advances in mathematical morphology applied to geoscience and remote sensing, *IEEE Transactions on Geoscience and Remote Sensing*, 40(9):2042–2055.

Soille, P., 2003. *Morphological Image Analysis - Principles and Applications*, Second edition, Berlin, Germany: Springer Verlag.

Sriwongsitanon, N., H. Gao, H.H.G. Savenije, E. Maekan, S. Saengsawang, and S. Thianpopirug, 2016. Comparing the Normalized Difference Infrared Index (NDII) with root zone storage in a lumped conceptual model, *Hydrology and Earth System Sciences*, 20(8):3361-3377.

Stehman, S.V., 1996. Estimating the kappa coefficient and its variance under stratified random sampling, *Photogrammetric Engineering & Remote Sensing*, 62(4):401–407.

Sternberg, S.R., 1986. Grayscale morphology, *Computer Vision, Graphics, and Image Processing*, 35:333–355.

Tarabalka, Y., J. Chanussot, and J.A. Benediktsson, 2010. Segmentation and classification of hyperspectral images using watershed transformation, *Pattern Recognition*, 40:2367–2379.

Tucker, C.J., 1980. Remote sensing of leaf water content in the near infrared, *Remote Sensing of Environment*,, 7:1395–1416.

Ullah, S., T.A. Groen, M. Schlerf, A.K. Skidmore, W. Nieuwenhuis, and C. Vaiphasa, 2012. Using a genetic algorithm as an optimal band selector in the mid and thermal infrared (2.5 –14 nm) to discriminate vegetation species, *Sensors*, 12:8775–8769.

Varshney, P.K., and M.K. Arora, 2004. *Advanced Image Processing Techniques for Remotely Sensed Hyperspectral Data*, Springer Verlag, 323 p.

Walther, D., and C. Koch, 2006. Modeling attention to salient proto-objects, *Neural Networks*, 19(9):1395–1407.

Wang, L., and J.J. Qu, 2007. NMDI: A normalized multi-band drought index for monitoring soil and vegetation moisture with satellite remote sensing, *Geophysical Research Letters*, 34(20).

Wang, Q., G. Zhu, and Y. Yuan, 2013. Multi-spectral dataset and its application in saliency detection, *Computer Vision and Image Understanding*, 117:1748–1754.

Yoon, S.C., and B. Park, 2015. Hyperspectral image processing methods, *Hyperspectral Imaging Technology in Food and Agriculture Part of the Series Food Engineering Series*, pp. 81– 101.

Zandler, H., A. Brenning, and C. Samimi, 2015. Potential of space-borne hyperspectral data for biomass quantification in an arid environment: Advantages and limitations, *Remote Sensing*, 7(4):4555–4580.

Zhang, H., H. Peng, M.D. Fairchild, and E.D. Montag, 2008. Hyperspectral image visualization based on a human visual model, *Human Vision and Electronic Imaging XIII* (Bernice E. Rogowitz, and Thrasyvoulos N. Pappas, editors) 68060N, 1–9.

Zhang, L., X. Lv, and X. Liang, 2017. Saliency analysis via hyperparameter sparse representation and energy distribution optimization for remote sensing images, *Remote Sensing*, 9:636.

Zhuo, L., J. Zheng, F. Wang, X. Li, B. Ai, and J. Qian, 2008. A genetic algorithm based wrapper feature selection method for classification of hyperspectral images using support vector machine, *Proceedings of the Geoinformation Joint Conference on GIS Built Environmentand Classification of Remote Sensing Images*, 7147:397–402.